Continuum Twisted Tower Origami Landing Gear for Drones
Design, Modelling and Experiments

Ramirez, Jane Pauline; Dux, Rafael; Hamaza, Salua

DOI
10.1109/RoboSoft63089.2025.11020912

Publication date
2025

Document Version
Final published version

Published in
2025 IEEE 8th International Conference on Soft Robotics, RoboSoft 2025

Continuum Twisted Tower Origami Landing Gear for Drones: Design, Modelling and Experiments

Jane Pauline Ramirez†, Rafael Dux†, Salua Hamaza

2025 IEEE 8th International Conference on Soft Robotics (RoboSoft) | 979-8-3315-2020-5/25/$31.00 ©2025 IEEE | DOI: 10.1109/RoboSoft63089.2025.11020912

***Abstract*— With advancements in drones' perception and control, the demand for enhanced mechanical design and integrated physical intelligence in these robots continues to grow. Effective landing gear systems are essential for preserving the integrity of agile, modern drones, where a careful combination of weight, durability, and complexity must be achieved. In this paper, we design, model and validate a continuum twisted tower origami to serve as a shock-absorbing landing gear for drones. Multiple different configurations with varying number of sides in the base and varying heights were 3D printed with a flexible material as monolithic structures. Characterization was performed using quasi-static testing and drone landing impact force measurements. The shock absorption was successfully demonstrated with a reduction of the total impact force of up to 75% for one of the tested configurations compared to a rigid landing gear during drop testing. Taller landing gears led to better impact force reduction, however with more units the whole structure bends excessively. The presented framework allows for scaling the landing structure in multiple ways, enabling the adaption to different drone platforms in the future, while keeping a single-material 3D-printing process without the need for further assembly.**

I. INTRODUCTION

NASA's *Ingenuity* helicopter—the first to achieve extraterrestrial powered flight—has concluded its mission on Mars after sustaining rotor-blade damage from hard landing, rendering it incapable of further flight [1]. This event highlights the necessity for advancements in developing aerial systems featuring physical intelligence like drones that can morphologically adapt to their environment with minimal computational and control requirements [2]. Such innovations would enhance drones' resilience and operational effectiveness in extreme terrestrial environments or Space [3].

Unmanned aerial vehicles (UAVs) that utilise vertical take-off and landing typically employ rigid landing gears, which can be insufficient for very hard landings as significant force is transmitted to the UAV's structure, damaging sensitive equipment and electronics. To address these issues, origami-inspired designs leverage shape-morphing abilities to create innovative structures that effectively respond to external forces. For example, [4] proposes a landing gear for drones employing origami-inspired structures. Their design incorporates 3D-printed Sarrus shock absorbers and soft landing pads, reducing the impact forces by up to 540 N for a 2 kg drone. Other examples are from [5], [6], [7], where instead the origami design serves as a protective enclosure around the propellers against lateral impacts during flight.

Fig. 1. A continuum twisted tower origami landing gear made of 4-stack hexahedric units mounted on a drone.

The ability to change shape or reconfigurability has been exploited for other applications as well, such as an origami-inspired folding arm used to access confined spaces [8]. Mechanisms exhibiting spring-like behavior under compression are potential candidates, as explored by [9], [10], [11] in their study of the Kresling origami for use as a robot arm. Another spring-like mechanisms, the twisted tower origami, has been utilised in robotic arms [12] and a three-finger gripper [13], showcasing interesting deformation behavior while maintaining a simpler structure than the Kresling origami. To avoid manual folding, 3D printing is often used for manufacturing these complex structures. However, producing relevant 3D printed designs frequently relies on expensive PolyJet printers for multi-material prints [11], [13] or requires the assembly of multiple parts [4], [10].

This paper presents a compliant landing gear for drones that absorbs impact, based on the origami twisted tower design, see Fig. 1. The contributions of the paper include:

- A manufacturing methodology enabling the 3D printing of the twisted tower origami mechanism as a single, monolithic structure using single-material fused deposition modeling.
- A buckling analysis of a column of a four-sided origami structure to measure deformation.
- Characterisation of different configurations through quasi-static testing to obtain force-displacement curves.
- Drop tests of a drone equipped with the landing structure to quantify the impact force reduction of the origami landing gear.

† These authors contributed equally to this work. Biomorphic Intelligence Lab, Dept. of Control & Operations, Faculty of Aerospace Engineering, TU Delft, The Netherlands. Contact: j.p.rramirez@tudelft.nl

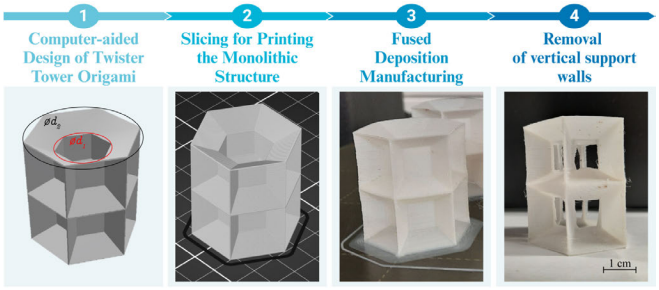

Fig. 2. Manufacturing process of the monolithic origami structure. (1) Parametrised CAD design based on inner diameter d_1, outer diameter d_2 and panel thickness t. (2) Slicing of the geometry to 3D-printer readable file. (3) 3D printing on an ORIGINAL PRUSA i3 MK3S+. (4) Removal of the vertical support walls with a cutter.

II. DESIGN

The design of aircraft landing systems depends on several factors, including sink speed, landing gear load factor, stroke, dynamic impact energy, and weight [14]. For micro-UAV systems, weight is a critical consideration and can be minimized by incorporating thin structural designs. At the same time, dynamic landing impact energy and stroke can be effectively managed through geometries capable of withstanding loads during deformation. We infer that stacking configurations will improve performance.

The manufacturing process using fused deposition modeling of thermoplastic urethane (TPU) is illustrated in Fig. 2. The dimensions chosen result in single- and double-wall layers, eliminating the need for infill. Many layers consist of two concentric loops following slicing. To ensure optimal overlap between layers, the G-Code was post-processed to reorder the two loops when necessary, with the loop having the most overlap printed first.[1] Printed samples included vertical support walls, which were removed using a cutter.

III. MODELLING

A. Geometry

The twisted tower design takes the shape of an $(m \geq 3)$-sided regular polygon in the top view, where m is an adjustable parameter. Each wall is an isosceles trapezoid of identical dimensions. m vertical walls form the vertices of the polygon, with two sets of m walls connecting and enclosing the structure at the top and bottom, forming radial symmetry in the design. The geometry is parametrised by the diameters d_1 and d_2 of the circumscribed circles of the inner and outer polygons, as shown in Fig. 2.

Any number n of these layers may be stacked on top of each other. Two adjacent layers can rotate in either the same or opposite directions. If the top and bottom faces are fixed relative to each other when the assembly is compressed, an even number of layers n must be selected, ensuring that an equal number of layers rotate in the clockwise and counterclockwise directions alternately.

[1]Source code available at https://github.com/BioMorphic-Intelligence-Lab/Twisted-Tower-Origami-Landing-Gear

TABLE I

SPECIFICATIONS OF TWISTED TOWER ORIGAMI SAMPLES

Number of layers n	2			4	6	8
Number of sides m	4	6	8	6		
Thickness t (mm)	0.4					
Inner diameter d_1 (mm)	20					
Outer diameter d_2 (mm)	40					
Height h (mm)	58	40	32	80	120	160
Mass m (g)	2.7	2.8	2.7	5.5	8.3	11.0

In this study, several design configurations have been explored, as detailed in Table I. For the two-layer case ($n = 2$), variations with tetrahedric, hexahedric, and octahedric geometries ($m = 4, 6, 8$) are tested. Higher layering configurations ($n = 4, 6, 8$) are also considered for the hexahedric design ($m = 6$). The diameters and wall thicknesses remain constant across these configurations.

B. Kinematics

The kinematics of the twisted tower, shown in Fig. 3, have been previously studied in the literature [13], [15], [16], [17]. We adopt Wang's [16] generalized kinematics for an m-sided polygon with r_1 as the radius of the inscribed circle for the center polygon, where the height h is primarily determined by the vertical segments, and the twisting angle is denoted by θ:

$$\theta_i = \pm \left(\frac{2\pi}{m} - \epsilon_\theta \right) \tag{1}$$

In this analysis, all trapezoids are treated as rigid walls, while the connections between adjacent trapezoids function as flexible hinges. The structure generates vertical motion by twisting along the center axis, causing the vertical walls to rotate and align with the horizontal walls. Consequently, a layer can fully collapse when rotated by twist angle of:

$$-2\pi/m + \epsilon_\theta \leq \theta_i \leq 2\pi/m - \epsilon_\theta \tag{2}$$

where ϵ_θ is small angle because of the panel thickness upon full collapse. With the assumption that the top and bottom plates remain parallel, the resulting linear distance l_i is

$$l_i = h - \frac{mh}{2\pi}|\theta_i| \tag{3}$$

$$l_i = h - \frac{mh}{2\pi}\left(\frac{2\pi}{m} - \epsilon_\theta \right) := \epsilon_d \tag{4}$$

The bending angle ϕ_i is limited to $0 \leq \phi_i \leq \phi_i^{max}$

$$\phi_i^{max} = 2sin^{-1}\left(\frac{l_i - e_d}{4r_1} \right) \tag{5}$$

The translation then becomes:

$$d_i = l_i - 2r_i sin\frac{\phi_i}{2} \tag{6}$$

The transformation matrix for stacked origami units is:

$$T = T_1 T_2 ... T_{n-1} T_n = \prod_{i=1}^{n} T_i \tag{7}$$

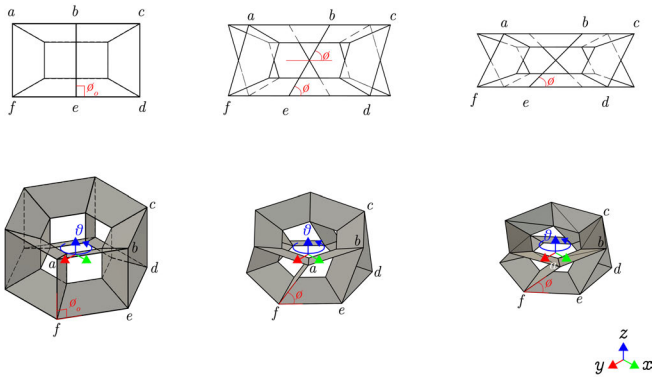

Fig. 3. Kinematics of the mechanism upon twisting along the z-axis with θ. The top reference frame is shown with the column as it hinges by ϕ, until the top and bottom plates' distance d reaches the minimum.

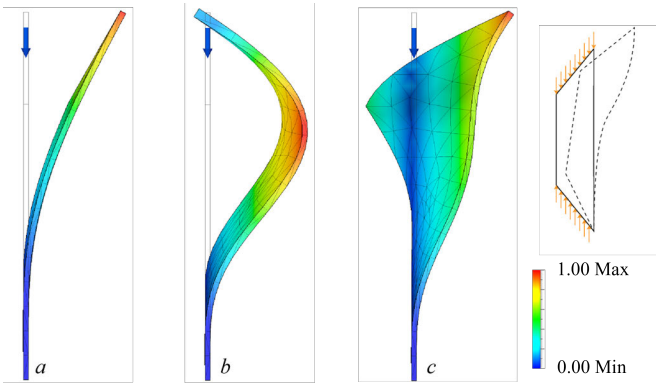

Fig. 4. Column buckling analysis of a 4-sided rubber origami column. (a) First eigenmode (b) Second eigenmode (c) Third eigenmode. Figures show side views with a distributed load on the top. Maximum deformation is 25% of the model size.

where the coordinate frames are centered in the bottom disc from $(i-1)^{th}$ layer to the i^{th} layer. The rigid body transformation where $\beta_i = \theta_i + \alpha_i$ and $c = cos, s = sin$ is

$$T_i = \begin{pmatrix} s\beta_i s\alpha_i + c\beta_i c\alpha_i c\phi_i & c\beta_i c\phi_i s\alpha_i - s\beta_i c\alpha_i & c\beta_i s\phi_i & d_i s\frac{\phi_i}{2} c\beta_i \\ s\beta_i s\alpha_i c\phi_i - c\beta_i s\alpha_i & c\beta_i c\alpha_i + s\beta_i c\phi_i s\alpha_i & s\beta_i s\phi_i & d_i s\frac{\phi_i}{2} s\beta_i \\ -c\alpha_i s\phi_i & -s\alpha_i s\phi_i & c\phi_i & d_i c\frac{\phi_i}{2} \\ 0 & 0 & 0 & 1 \end{pmatrix} \tag{8}$$

C. Structural Buckling

In the previous kinematic analysis, we have assumed that the faces follow deformation in rigid components. However, since this is a monolithic structure, the structures will buckle with compressive stress hinging along the top and bottom panels that enables twisting of the origami structure. Axial load will cause bending deformations and buckling to the vertical segments that causes the unit to have a screwing motion or a torsional deformation about the z-axis. We used the Eigenvalue buckling analysis, shown in Fig. 4 to investigate mode shapes for TPU, under the simplified isotropic condition to have an insight on how the structure buckles. To setup the analysis, we have isolated a column of a four-sided origami which is the simplest case with respect to the number of sides in Fusion 360. The following assumptions are used: fully elastic buckling assumption, materials are below yield stress. The bottom face has a fixed constraint. The 2.5N = 10 N/ 4 columns load is applied to the global z-axis distributed over the top surface. The simulation is made up of 348 tetrahedral elements with 801 nodes. The Euler equation to calculate critical buckling load is $F = \frac{\pi^2 EI}{(kh)^2}$ where F = critical buckling force, E = modulus of elasticity, I = area moment of inertia of the cross section, h = unsupported length of the column and k = column effective length factor.

IV. RESULTS

To evaluate the design, two experiments were done. First, static testing showed the force-displacement relationship of the origami structure. Second, drop testing of a drone equipped with landing gears is done to assess the mechanism's performance under realistic conditions through measuring maximum impact forces.

A. Static Testing

The analysis of the compression tests begins with a comparison of different geometries for 2-layer samples, followed by an investigation into the effect of varying layer counts for hexahedric samples. Stiffness characterisation of individual samples was conducted using a 10 kN Zwick static testing machine equipped with a 10 N Zwick load cell. Each sample was compressed between two flat plates at a rate of 3 mm/s. All samples were produced, stored, and tested under ambient conditions.

1) Two-layer Samples: Fig. 5 presents the force-displacement relationship of 2-layer samples with 4, 6 & 8 sides, accompanied by pictures of the samples taken during the compression test. The static testing revealed highly nonlinear dynamics. During compression, there is a short phase of high stiffness in the beginning, where the structure is not yet moving significantly. This is followed by a plateau of quasi-zero stiffness, where the restoring force is constant over a large deformation. The structure thus exerts a constant resistance to compression in this regime. During this second phase, the middle plane(s) rotate, leading to the contraction of the mechanism. Contrary to the theoretical description, the bending is not localized in the hinges but occurs distributed along the length of the vertical walls. Simulations on the effect of buckling in this case can be seen in Fig. 4 in the previous section. This does not change the general behaviour of the mechanism, though, and the origami structure collapses close to the theoretical kinematics. Once the rotational movement of the two layers approaches its theoretical maximum, the structure transitions to a third phase of relatively high stiffness. The limited flexibility of the hinges and the non-zero thickness of the walls leading to self-contact of the structure restrict further movement in this phase. The magnitude of the force plateau is 2.0 N for the tetrahedric sample, 2.8 N for the hexahedric, and 4.0 N

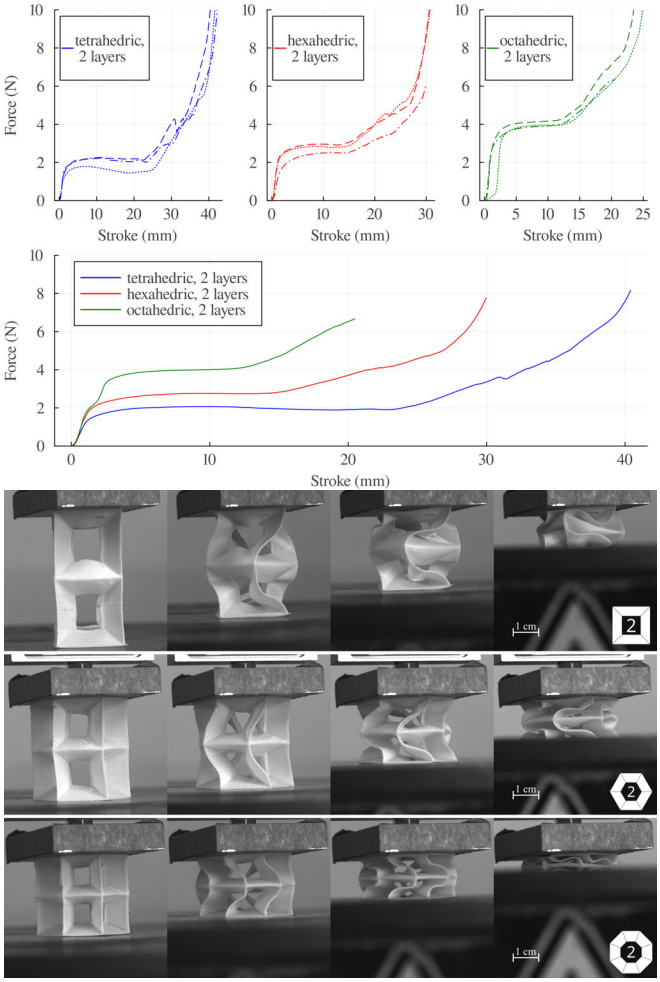

Fig. 5. Static compression tests were performed on 2-layer tetrahedric, hexahedric, and octahedric samples, with individual (dashed lines) and average responses recorded across three samples per geometry. Under axial load, columns deform, causing top-layer rotation along the z-axis, followed by further compression.

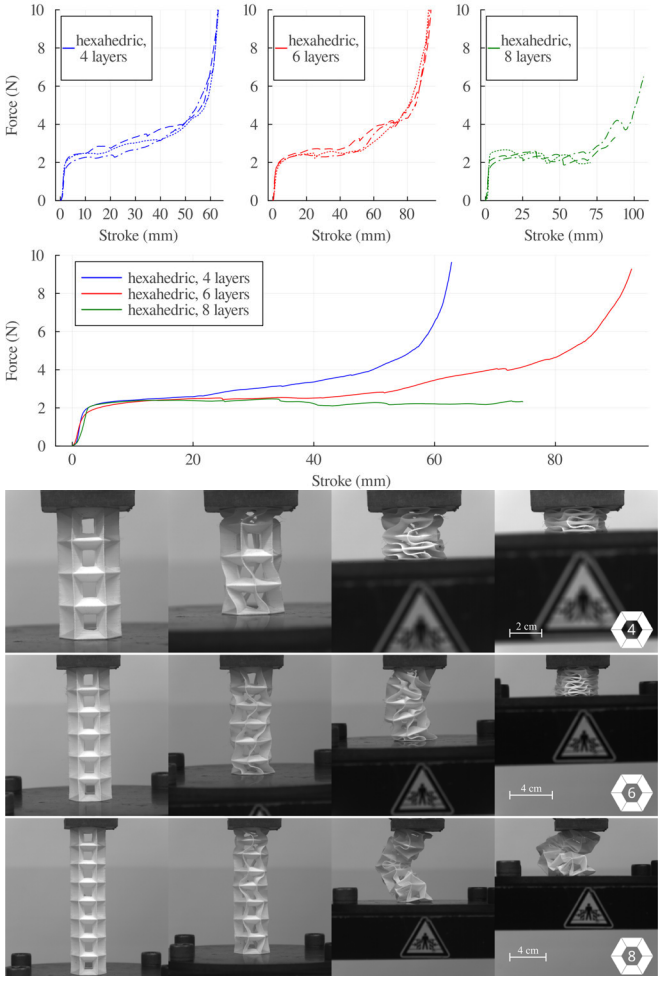

Fig. 6. Static compression tests on 4-, 6-, and 8-layer hexahedric samples, with individual (dashed lines) and average responses across three samples per configuration. Results show that increasing stacked layers raises overall height, increasing susceptibility to buckling.

for octahedric. We observe that the magnitude of the force plateau increases with the number of sides m because most of the resistance to movement is localized in the bending of the m vertical walls, especially for low displacements. Except for the different magnitude of the force plateau, samples with a different number of sides m show similar behaviour in the force-displacement relationship.

2) Hexahedric 4-, 6- & 8-layer Samples: Fig. 6 presents the force-displacement relationship of hexahedric samples with 4, 6 & 8 layers, accompanied by pictures of the samples taken during the compression test. Due to the observed similarity of the overall behaviour of the tetrahedric, hexahedric and octahedric 2-layer samples, only the intermediate, i.e. the hexahedric, design is tested with different heights. During testing, it can be observed that not all layers collapse equally at the same time but that some layers get compressed almost completely first, before significant movement is initiated in others. This is probably due to manufacturing variations, which induce a slightly different plateau magnitude of individual layers. The collapse is happening in the quasi-zero stiffness regime, so small variations can have a bigger impact. Similarly, the direction of movement of the intermediate layers does not follow a clear order and is thus presumably also defect-determined, given that the structure is radially symmetric. During the compression test of the 6-layer samples, considerable column buckling of the whole structure is present, presenting itself by an off-axis movement of the middle layers. However, upon further compression, the structure comes back to its original form. When compressing the 8-layer samples, the overall column buckling becomes dominant and the tests are stopped manually. To compare samples of different height, Fig. 7 also presents the relationship between force and strain (stroke / initial height), for hexahedric samples ($m = 6$). All tested heights, 2, 4, 6 & 8 layers, show very similar behaviour, especially at low displacements. This behaviour is consistent with the traditional model of springs in series, and thus promises to extrapolate to other geometries as well. The equivalent spring constant (k_{eq}) for n units, with: $F_{eq} = F_1 = ... = F_n$, is $\frac{1}{k_{eq}} = \sum \frac{1}{k_n}$.

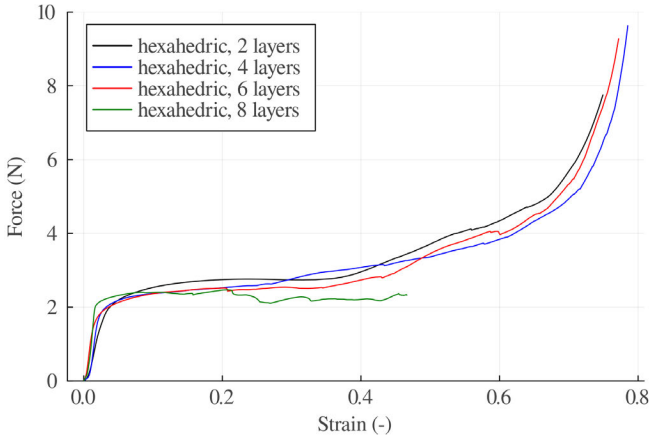

Fig. 7. Strain comparison of 2-, 4-, 6-, and 8-layer hexahedric samples. This figure demonstrates that the behaviour of individual hexahedric units remains consistent across varying layer counts, suggesting that results can be extrapolated to larger monolithic stacks composed of multiple units.

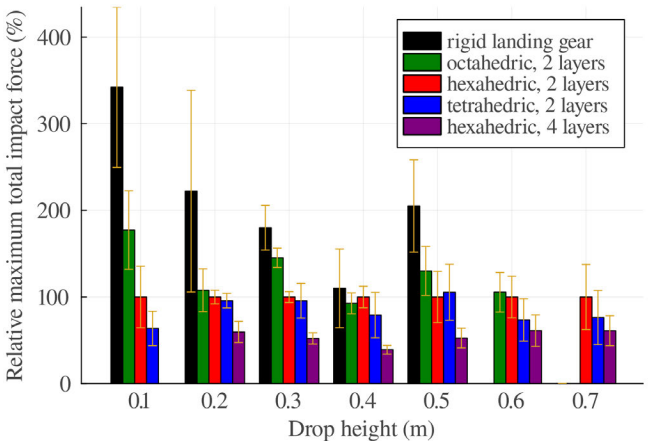

Fig. 8. Maximum total relative impact force as measured by ground-mounted force sensor during drop testing. Bar chart, with error bars shown in yellow, representing the relative magnitude compared to the hexahedric 2-layer samples shows that the 4-layer hexahedric decreased the force by 75% compared to the rigid landing gear.

B. Drop Testing and Impact Force Characterisation

Impact force characterization includes images of the landing gear during impact and an analysis of the drone's trajectory post-drop. The impact force was measured using an ATI Mini45 F/T sensor (7000 Hz, 1/16 N resolution), mounted on a 3D-printed PLA bottom plate for stability. A 300×300×10 mm PLA top plate served as the landing pad, attached to the sensor.

A custom 3D-printed drone frame allowed easy landing gear attachment, with motors mounted for realistic weight distribution (total mass: 250g). Tested landing gears included 2-layer tetrahedric, hexahedric, octahedric, and 4-layer hexahedric structures. A baseline test was performed without origami structures, simulating a rigid landing gear. The drone was dropped from defined heights, simulating a sudden power loss scenario. Drop heights started at 0.1 m (0.2 m for 4-layer samples) and increased in 0.1 m increments until the force sensor's range was maxed out. Each configuration was tested with three drops, and drone position was tracked at 120 Hz using an OptiTrack motion capture system.

Impact forces were compared to the hexahedric 2-layer design (Fig. 8). Origami landing gears significantly reduced the impact force versus the rigid baseline. Among the 2-layer designs, tetrahedric performed the best, followed by hexahedric and octahedric. Taller and less stiff structures showed better reduction in impact force. The 4-layer hexahedric design performed best, reducing force by 40% compared to its 2-layer counterpart at 0.7 m and by 75% versus the rigid baseline at 0.5 m. This was achieved with a landing gear-to-total-mass ratio of less than 9%. Upon impact, the drone bounces shortly before coming to rest on the landing pad. Example of the projected 2D trajectories of the drone dropping from 0.3 m height are shown in Fig. 9. The drone frames equipped with the shock-absorbing landing gears show considerably more bouncing than the rigid baseline, due to the energy stored during shock-absorption being partially put back into the system.

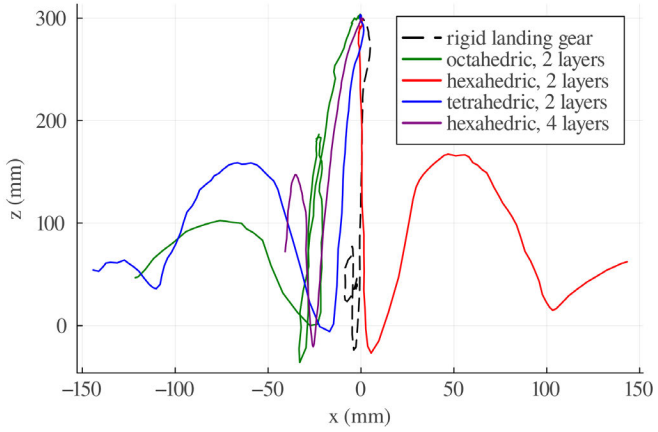

Fig. 9. Example 2D-projected trajectories of one drop from 0.3 m height showing the dissipation of forces through the compliant landing gear, as compared to the rigid landing gear baseline.

Slow-motion video recordings confirm that origami landing gears deform dynamically as in static tests. Fig. 10 shows the increasing instability of taller structures, with the bottom of 4-layer landing gears exhibiting significant lateral displacement. Preliminary tests found 4 layers to be the maximum stable height, as taller designs showed excessive instability. This aligns with quasi-static testing, where 6- and 8-layer hexahedric samples exhibited column buckling. Thus, a trade-off exists between greater impact force reduction and increased instability. Taller landing gears compressed less, with the 4-layer hexahedric retaining the most height, while 2-layer versions compressed more. Among them, octahedric compressed almost fully, while hexahedric and tetrahedric retained slightly more height, correlating with their impact force reduction.

C. Design Considerations

Relating the results from the static testing and the drop testing, a method for designing a required impact force re-

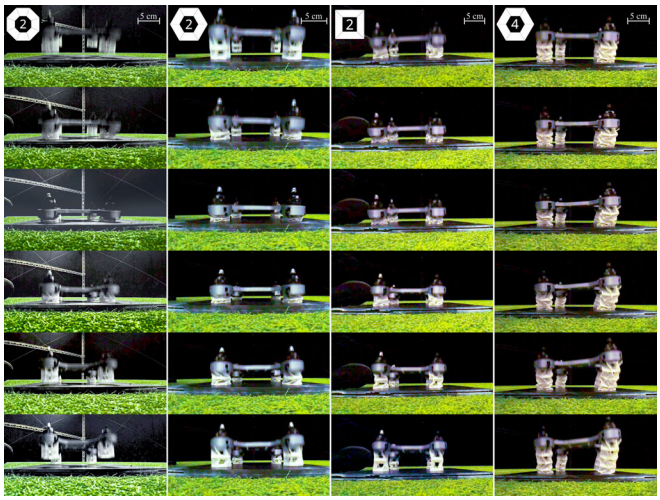

Fig. 10. Drop testing experiments of octahedric 2-layer, hexahedric 2-layer, tetrahedric 2-layer and hexahedric 4-layer samples landing from 0.3 m drop height. Pictures spaced 1/100 s apart.

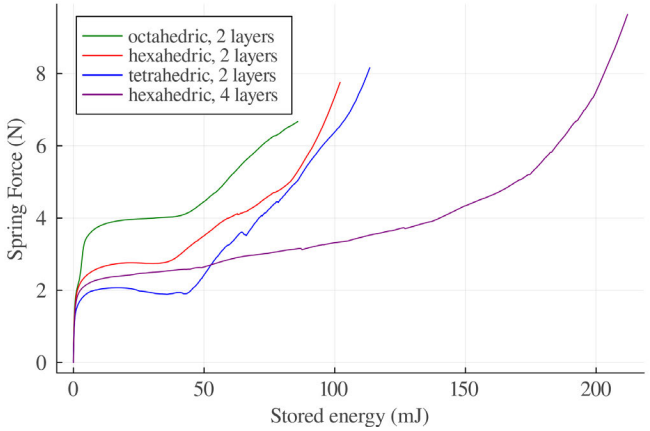

Fig. 11. Spring force of the landing gear as a function of the stored energy. Lower spring force for a specific stored energy is in agreement with higher impact force reduction during drop testing as shown in Fig. 8.

duction can be devised by considering the energies involved during impact. Modelling the landing gear as a spring and assuming no dissipative losses, due to the conservation of energy, the maximum spring potential energy $SE = \int Fdx$ is equal to the kinetic energy $KE = 0.5mv^2$ just before impact which is equal to the gravitational potential energy $PE = mgh$. The maximum impact force can thus be estimated by the restoring spring force when all the initial gravitational potential energy is converted into the spring potential energy of the landing gear, of which the relation is shown in Fig. 11 using the results from static testing. The design of a specific landing gear system can then be performed as a function of several parameters: total drone mass m_d, drop height h_d, number of individual landing gears, Factor of Safety FS and the geometry-dependent spring characteristics.

V. CONCLUSION

This paper presents the design and testing of a continuum and compliant twisted tower origami-based landing gear. Two-layer samples of different geometries (tetrahedric, hexahedric, octahedric) and hexahedric samples of different heights (4, 6, 8 layers) underwent stiffness and impact force characterisation. The samples presented highly non-linear dynamics. Mounted on a drone, a total impact force reduction of up to 75% was observed during drop testing, when comparing the hexahedric 4-layer landing gear to a rigid landing gear at 0.5 m drop height. These dynamics are achieved with a simple fabrication approach as the mechanism can be 3D printed with a single material on a widely-, and cheaply-available fused deposition modeling printer. As the entire design is parametrised, it offers the opportunity for scaling from small to large quadrocopters. Through choosing the flexible material and the wall thickness, the stiffness and related properties can additionally be modulated.

REFERENCES

[1] M. Wall, "Ingenuity Mars helicopter snapped rotor blade during hard landing last month (video, photo)," Feb. 2024.

[2] J. P. Ramirez, A. Bredenbeck, and S. Hamaza, "Bioinspired compliant limbs for robust landing of free-flying robots," in *17th Symposium on Advanced Space Technologies in Robotics and Automation*, ESA/ESTEC, 2023.

[3] J. P. Ramirez and S. Hamaza, "Multimodal locomotion: next generation aerial–terrestrial mobile robotics," *Advanced Intelligent Systems*, p. 2300327, 2023.

[4] K. Zhang, P. Chermprayong, D. Tzoumanikas, W. Li, M. Grimm, M. Smentoch, S. Leutenegger, and M. Kovac, "Bioinspired design of a landing system with soft shock absorbers for autonomous aerial robots," *Journal of Field Robotics*, vol. 36, no. 1, pp. 230–251, 2019.

[5] P. Sareh, P. Chermprayong, M. Emmanuelli, H. Nadeem, and M. Kovac, "Rotorigami: A rotary origami protective system for robotic rotorcraft," *Science Robotics*, vol. 3, no. 22, p. eaah5228, 2018.

[6] J. Shu and P. Chirarattananon, "A quadrotor with an origami-inspired protective mechanism," *IEEE Robotics and Automation Letters*, vol. 4, no. 4, pp. 3820–3827, 2019.

[7] C.-Y. Park, Y.-A. Lee, J. Jang, and M.-W. Han, "Origami and kirigami structure for impact energy absorption: Its application to drone guards," *Sensors*, vol. 23, no. 4, p. 2150, 2023.

[8] S.-J. Kim, D.-Y. Lee, G.-P. Jung, and K.-J. Cho, "An origami-inspired, self-locking robotic arm that can be folded flat," *Science Robotics*, vol. 3, no. 16, p. eaar2915, 2018.

[9] A. S. Dalaq and M. F. Daqaq, "Experimentally-validated computational modeling and characterization of the quasi-static behavior of functional 3d-printed origami-inspired springs," *Materials & Design*, vol. 216, p. 110541, 2022.

[10] L. Mena, J. Muñoz, C. A. Monje, and C. Balaguer, "Modular and self-scalable origami robot: A first approach," *Mathematics*, vol. 9, no. 12, p. 1324, 2021.

[11] S. Khazaaleh, R. Masana, and M. F. Daqaq, "Combining advanced 3d printing technologies with origami principles: A new paradigm for the design of functional, durable, and scalable springs," *Composites Part B: Engineering*, vol. 236, p. 109811, 2022.

[12] T. Liu, Y. Wang, and K. Lee, "Three-dimensional printable origami twisted tower: Design, fabrication, and robot embodiment," *IEEE Robotics and Automation Letters*, vol. 3, no. 1, pp. 116–123, 2017.

[13] K. Lee, Y. Wang, and C. Zheng, "Twister hand: Underactuated robotic gripper inspired by origami twisted tower," *IEEE Transactions on Robotics*, vol. 36, no. 2, pp. 488–500, 2020.

[14] N. S. Currey, *Aircraft landing gear design: principles and practices*. American Institute of Aeronautics and Astronautics, 1988.

[15] D. Jeong and K. Lee, "Design and analysis of an origami-based three-finger manipulator," *Robotica*, vol. 36, no. 2, pp. 261–274, 2018.

[16] Y. Wang and K. Lee, "3d-printed semi-soft mechanisms inspired by origami twisted tower," in *2017 NASA/ESA Conference on Adaptive Hardware and Systems (AHS)*, pp. 161–166, IEEE, 2017.

[17] F. Fei, Y. Leng, S. Xian, W. Dong, K. Yin, and G. Zhang, "Design of an origami crawling robot with reconfigurable sliding feet," *Applied Sciences*, vol. 12, no. 5, p. 2520, 2022.